Petroleum Science
https://doi.org/10.1007/s12182-020-00528-9

ORIGINAL PAPER

Pore structure characterization and its effect on methane adsorption in shale kerogen

Tian-Yu Wang[1,2] · Shou-Ceng Tian[1,2] · Qing-Ling Liu[3] · Gen-Sheng Li[1] · Mao Sheng[1,2] · Wen-Xi Ren[1,4] · Pan-Pan Zhang[1,2]

Received: 3 February 2020 / Accepted: 22 October 2020

Abstract

Pore structure characterization and its effect on methane adsorption on shale kerogen are crucial to understanding the fundamental mechanisms of gas storage, transport, and reserves evaluation. In this study, we use 3D scanning confocal microscopy, scanning electron microscopy (SEM), X-ray nano-computed tomography (nano-CT), and low-pressure N_2 adsorption analysis to analyze the pore structures of the shale. Additionally, the adsorption behavior of methane on shales with different pore structures is investigated by molecular simulations. The results show that the SEM image of the shale sample obviously displays four different pore shapes, including slit pore, square pore, triangle pore, and circle pore. The average coordination number is 4.21 and the distribution of coordination numbers demonstrates that pores in the shale have high connectivity. Compared with the adsorption capacity of methane on triangle pores, the adsorption capacity on slit pore, square pore, and circle pore are reduced by 9.86%, 8.55%, and 6.12%, respectively. With increasing pressure, these acute wedges fill in a manner different from the right or obtuse angles in the other pores. This study offers a quantitative understanding of the effect of pore structure on methane adsorption in the shale and provides better insight into the evaluation of gas storage in geologic shale reservoirs.

Keywords Shale · Methane adsorption · Pore structure · Kerogen · Molecular simulation

1 Introduction

The extraction of gas from shale is regarded as an energy game-changer (Hughes 2013). As a transition fuel, shale gas offsets reducing of conventional gas production (Vidic et al. 2013). Horizontal drilling coupled with multi-stage hydraulic fracturing makes it possible to extract hydrocarbons from shale reservoirs (Ren et al. 2016; Shi et al. 2019). Gas in shale reservoirs mainly exists in three forms: free gas, adsorbed gas, and dissolved gas. Particularly, about 20%−85% of the total gas-in-place is adsorbed gas (Curtis 2002). In shale gas production, the desorption of adsorbed gas can compensate for the loss of free gas, which is a significant reason that shale gas maintains long-term stable production (Wang et al. 2019a). Therefore, understanding the adsorption of hydrocarbons in shale is essential for reliable resource assessment and shale gas recovery.

In general, pores in shale are much smaller than those in conventional sandstone reservoirs (Loucks et al. 2012; Shen et al. 2019). Pore structure characterization has attracted great attention. Nitrogen adsorption tests are used

Edited by Yan-Hua Sun

Electronic supplementary material The online version of this article (https://doi.org/10.1007/s12182-020-00528-9) contains supplementary material, which is available to authorized users.

✉ Shou-Ceng Tian
tscsydx@163.com

[1] State Key Laboratory of Petroleum Resources and Prospecting, China University of Petroleum (Beijing), Beijing 102249, China

[2] Harvard SEAS-CUPB Joint Laboratory on Petroleum Science, 29 Oxford Street, Cambridge, MA 02138, USA

[3] China National Oil and Gas Exploration and Development Company Ltd, Beijing 100034, China

[4] State Key Laboratory of Oil and Gas Reservoir Geology and Exploitation, Southwest Petroleum University, Chengdu 610500, China

Published online: 12 November 2020

to measure pore size distribution in shale samples (Feng et al. 2018; Groen et al. 2003). Also, the non-local-density functional theory is also used to characterize the pore structures in shale media (Wei et al. 2016). This is considered to be a more accurate method for pore characterization when taking the entire size distribution of nanopores into account. However, these methods of gas physisorption cannot identify the location of the pores. Small-angle neutron scattering and ultrasmall-angle neutron scattering techniques have been applied for understanding the porosity characteristics of the shale samples (Clarkson et al. 2013; Mastalerz et al. 2012a). Scanning electron microscopy (SEM) and atomic force microscopy (AFM) are also used to characterize the pores in the sample (Javadpour et al. 2012; Tian et al. 2018; Tian et al. 2019). Although they can directly reveal the locations of the pores, the connectivity of the pores cannot be revealed by SEM and AFM. Nano-CT and nano-transmission X-ray microscopy are sufficient methods to quantify nanometer pore structures in shale (Tiwari et al. 2013). Each of these methods has its own advantage and deficiency. In this work, both indirect and direct methods are used on shale samples to characterize the pore structures.

Adsorbed gas content is an essential parameter to predict the production of shale reservoirs (Chen et al. 2019; Zhou et al. 2018). Methane adsorption has attracted much attention to understanding the storage and adsorption mechanisms in shale (Ren et al. 2017; Singh and Cai 2018). Many scholars have done much experimental research about this problem (Gensterblum et al. 2014; Yuan et al. 2014). Pressure as an external condition is a key parameter of methane adsorption on shale. Due to the high-pressure geological conditions of shale reservoirs, methane adsorption measured at relatively low pressures is generally used to predict the adsorption at high pressures (Ross and Bustin 2008). Accurate measurement of the high-pressure adsorption of methane on shale poses a long-stand challenge. Therefore, molecular simulation is recently used to study the adsorption mechanisms of methane on shale media (Jin and Firoozabadi 2014; Xiong et al. 2017; Yuan et al. 2015). Grand canonical Monte Carlo (GCMC) simulation is used to investigate the effect of O/C ratio and oxygen-containing chemical groups on methane adsorption capacities in graphitic slits (Liu and Wilcox 2012). The moisture content reduces methane adsorption on shale (Zhao et al. 2017). The moisture content in shale reservoirs is increased due to hydraulic fracturing. Therefore, the pores and throats can be blocked by water, which reduces the methane adsorption capacity on shale media (Krooss et al. 2002). Also note that shale with more water content has lower gas adsorption than that without water in the pores because water occupied some of the adsorption sites in shale (Zou et al. 2018). The influence of pore structures on methane adsorption also attracts the attention of the researchers. Song et al. (2018) investigated the influences of different carbon pore structures on methane adsorption by GCMC simulations. In our previous work, we also developed a model, which considers the matrix and slit nanopores of kerogen, to describe the real shale kerogen nanopores and quantify CO_2/CH_4 competitive adsorption (Wang et al. 2018b).

Although great achievements of methane adsorption on shale have been made, there are still some problems because of the complex adsorption behavior. The first problem is lacking comprehensive research on pore structure characterization. Real pores and throats in shale media have complex and variable cross sections. However, they are usually approximated as a cylinder of constant cross section. The second problem involves the effect of the pore structure on methane adsorption in shale kerogen. Often shale adsorption ability is represented by the adsorption of methane against the specific surface area or pore volume (Wu et al. 2015). The ability is also expressed by the adsorption capacity per weight of shale (Sharma et al. 2015; Zhai et al. 2014). However, the pore size has a great impact on the adsorption capability of methane on shale samples. In addition, the simple models for porous carbon materials, such as graphene slit and carbon nanotubes, cannot accurately describe the complex kerogen structure (Song et al. 2018). Therefore, comprehensive research is required to characterize the pore structure and investigate the effect of pore shape on methane adsorption.

In this work, we firstly use a 3D scanning confocal microscope to characterize the surface topography of shale samples. Then, a combination of the SEM and the energy dispersive X-ray spectrometry (EDS) is used to characterize the pore structure and detect various structural components of shale. X-ray nano-CT imaging is performed to quantify nanometer pore structures in shale. Low-pressure N_2 adsorption analysis is used to measure the specific surface area, average pore diameter, pore volume, and micro-pore volume of four shale samples. In addition, we use GCMC simulations to study the adsorption behavior of methane on shale with different pore shapes. Finally, we study the impacts of water content on the methane adsorption in different pores based on a more realistic model. The scientific significance of this work is that we provide an understanding of the effects of pore structure on methane adsorption from a microscopic perspective and quantify this effect to provide better insight into the evaluation of gas storage in geologic shale reservoirs.

2 Materials and methods

Shale samples were collected from Lower Silurian Longmaxi Formation, which has been the most successfully developed shale gas reservoir in China. The total organic

carbon (TOC) content of the shale samples is 5.71 wt%. The high energy argon ion beam was used to decrease the roughness of the shale surface. The topography and roughness of the shale surface were measured with a 3D scanning confocal microscope (KEYENCE VK-X100). The distributions of organic matter (OM) and inorganic matter (IOM) were observed with an SEM (Hitachi SU8010) under a high vacuum. The compositions of shale samples were analyzed by EDS. The nanostructures of shale samples were investigated with an X-ray nano-CT scanner (Ultra XRM-L200 CT, Xradia). A cylindrical shale block with a diameter of 65 μm was drilled for a CT scan. The scan time and exposure time were 32 h and 120 s, respectively. A cubic model, with a side length of 38.4 μm, was built through 3D reconstruction technology. Information about the pore distribution was determined using the Avizo Fire software, which can obtain the 3D pore structure of the sample. N_2 adsorption/desorption experiments were conducted with a Bel-Max high-end volumetric gas adsorption instrument. The BELSORP-max was used to analyze the surface area and pore size distribution.

3 Results and discussion

3.1 Surface topography and composition assessment

To make a careful observation, we use the high-energy argon ion beam to decrease the roughness of the shale surface. After that we use the 3D measurement system to characterize the shale surface topography. Figure 1a, b shows the surface topography and height distribution of the shale sample, which has a mean surface roughness of 0.785 μm. Furthermore, the microstructures and elemental distribution of the shale surface are observed by SEM and EDS. As can be seen in Fig. 1c, d, SEM images have shown that the distinction between the organic matter and inorganic matter is obvious, which indicates that shale is highly heterogeneous at the micro-scale. Carbon is a major component of the organic matter of shale, while the inorganic matter surface is rich in oxygen. The elemental distributions of oxygen, carbon, silicon, and aluminum are shown in Fig. 1e, h. On balance, the main elements of the shale sample are carbon, oxygen, silicon, and aluminum, as shown in Fig. S1 (see electronic supplementary material). A similar result is also presented by previous research (Wang et al. 2019b). However, these elements are slightly different in proportion for different shale samples. This is also because of the heterogeneity of shale gas reservoirs.

3.2 Analysis of pore characteristics

The size distribution and shape of shale pores and throats determine the reserves and transmission capacity of shale gas. Figure 2a plots the nano-CT image of a shale block with a diameter of 38.4 μm. The pore size distribution and shape factor are determined using the attribute extraction method. The red part in Fig. 2b represents the pores and throats. The largest maximal balls are identified as pores, while the smallest balls are throats (Dong and Blunt 2009). The pore network is simplified using the ball-and-stick model, and the parameters of pores and throats are obtained. The statistical sizes of pores and throats include their inscribed radius and shape factors. The statistical comparisons of the inscribed radius, shape factors of pores and throats are plotted in Fig. 2c-2d, respectively. The radii of most of the pores and throats are less than a micron, including the organic pores and inorganic pores in shale media. The peak values of the radii of pores and throats are 8.22×10^{-8} m and 1.46×10^{-7} m, respectively. The throat is a continuous channel between the nanopores and a key parameter of shale transport capacity.

The connectivity of the pore network is expressed by coordination numbers. The coordination numbers of pores and throats are shown in Fig. 3. The average coordination number is 4.21 and the distribution of coordination numbers demonstrates that the pores in shale samples have high connectivity (Zhang et al. 2015). The presence of pores with high connectivity may be attributed to the existence of more tortuous paths that join a large number of pores together (Al-Kharusi and Blunt 2007).

In the previous section, it has been shown that the shale samples have complicated pore structures. In this section, we are primarily concerned with the quantitative analysis of pore structure parameters. N_2 adsorption isotherms are used to measure the specific surface area, pore volume, average pore diameter, and micro-pore volume of four shale samples. N_2 adsorption isotherms of the four shale samples can be seen in Fig. 4. The adsorption and desorption isotherms are almost overlapped under relatively low pressures. However, with increasing relative pressure, the adsorption and desorption isotherms do not overlap, which results in a hysteresis loop. This is because the capillary condensation occurs within the meso-pores (Sing 1985). N_2 adsorption/desorption isotherms with hysteresis loops indicate that the shale samples contain both meso-pores and macro-pores (Xiong et al. 2015). Table 1 displays the pore structure parameters calculated by the Brunauer–Emmett–Teller method. The specific surface area is 9.83–22.84 m^2/g with an average value of 14.03 m^2/g, and the pore volume ranges from 1.34×10^{-2} to 2.27×10^{-2} cm^3/g with an average value of 1.61×10^{-2} cm^3/g. The average pore diameter and micro-pore volume

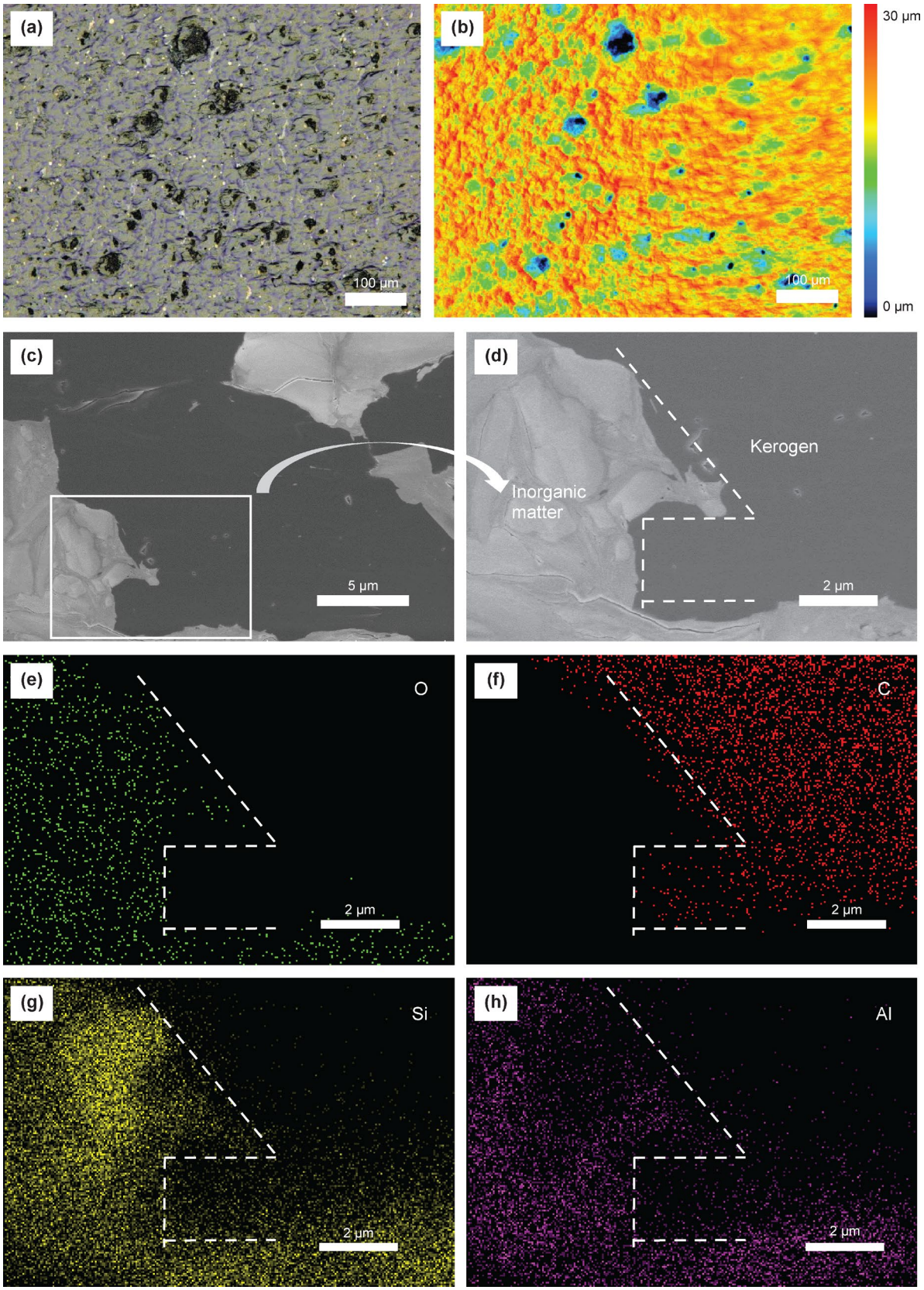

Fig. 1 **a** Surface topography of the shale sample; **b** Height distribution of the shale sample; **c** SEM image of the shale sample; **d** Local enlarged image of the shale sample; **e** EDX image of O element of the local enlarged image; **f** EDX image of C element of the local enlarged image; **g** EDX mapping of Si element of the local enlarged image; **h** EDX mapping of Al element of the local enlarged image

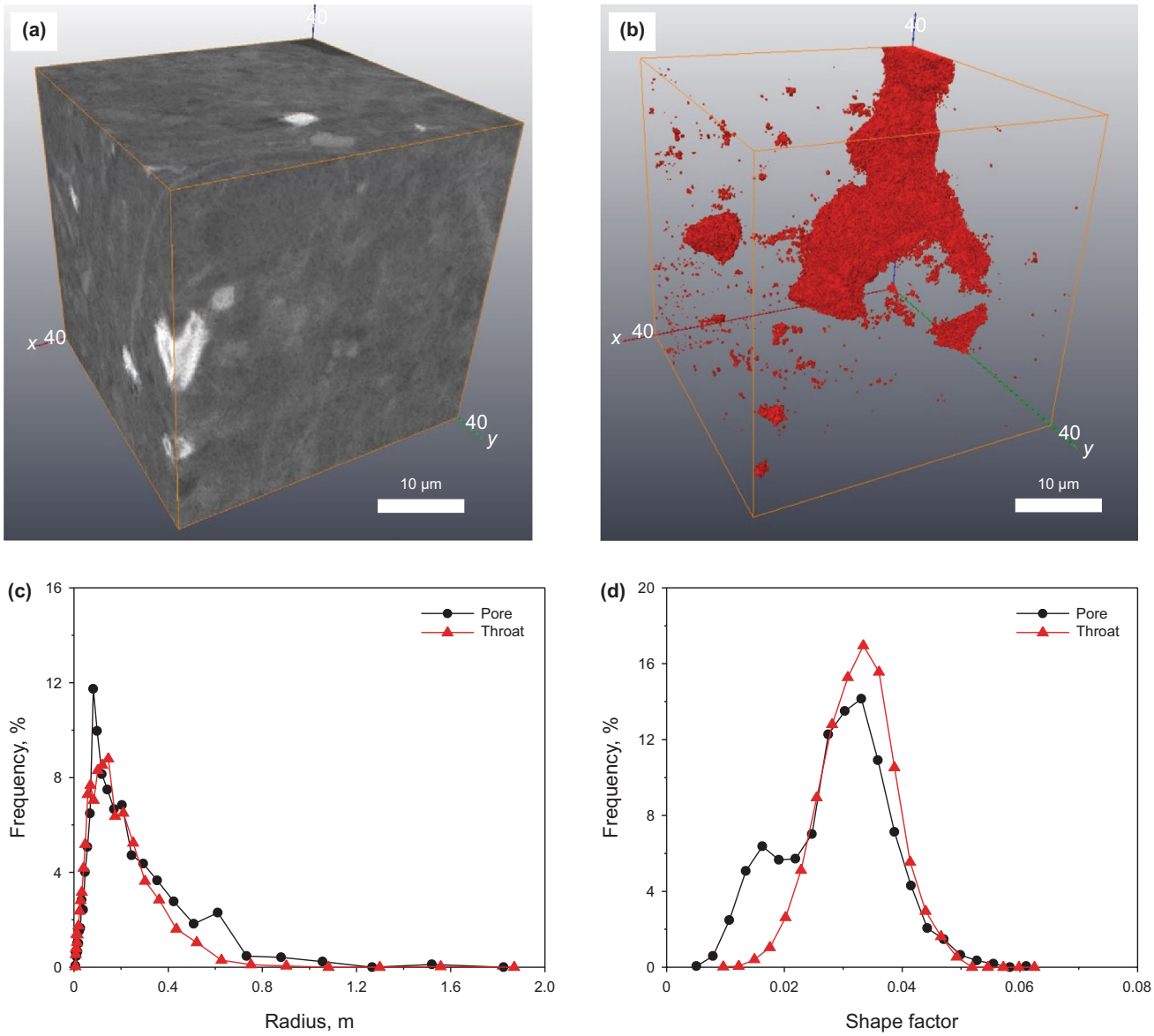

Fig. 2 **a** Nano-CT image of the shale sample; **b** Pore distribution in digital rock; **c** Size distributions of pores and throats; **d** Shape factor of pores and throats in digital shale

range from 3.97 to 5.44 nm with an average value of 4.785 nm and from 3.19×10^{-4} to 4.59×10^{-3} cm^3/g with an average value of 1.81×10^{-3} cm^3/g, respectively. Some previously published experimental data (Sun et al. 2016; Yang et al. 2016) are also included in Fig. 5 and it can be seen that the specific surface area positively correlates with the pore volume (Fig. 5a). In contrast, the average pore size is in a negative correlation to the pore volume and specific surface area (Fig. 5b, c), which is consistent with previous studies (Chalmers et al. 2012). In addition, the pore shape is also an important factor that affects the adsorption capacity of methane on shale, which can be observed directly from the SEM image, as shown in Fig. 6. The SEM image of the shale sample obviously displays four different pore shapes, including slit pore, square pore, triangle pore, and circle pore. We use GCMC simulations to study the adsorption behavior of methane on shale with these four pore shapes.

4 Molecular simulation

4.1 Models and methodology

The kerogen model is built by Ungerer et al. (2014) based on the experimental data (Kelemen et al. 2007), as shown in

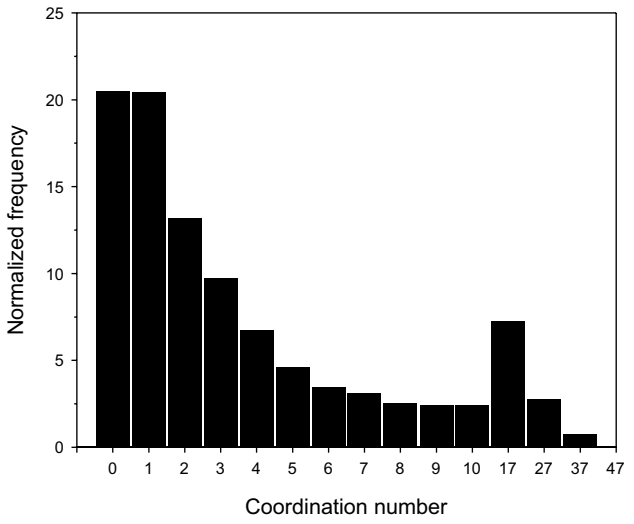

Fig. 3 Coordination numbers of the pores and throats in the shale sample

Fig. 7a. The composition of the kerogen is $C_{251}H_{385}O_{13}N_7S_3$. It is typical of kerogen deposited in excellent conditions of preservation, such as anoxic lacustrine environments, and it is classified as immature based on its hydrocarbon generation (Ungerer et al. 2014). The parameters of the molecular model match analytical data well with reasonable accuracy, as indicated in Table S1 (see electronic supplementary material). We use 10 kerogen molecules to build a kerogen cell, as shown in Fig. 7b. In our previous work, we have validated the molecular model with the experimental data from the literature (Wang et al. 2018b). The density is 1.097 g/cm^3, which is in agreement with the measured result ranging from 1.0 g/cm^3 to 1.15 g/cm^3 (Mastalerz et al. 2012b). In this work, we modify the kerogen model with different pore shapes compatible with SEM images. Figure 8 plots the kerogen models with different pore shapes. Different pore shapes have the same pore volume, which means the matrix volumes are the same. The diameter of the circle pore is 2 nm. The volume of the circle pore is 3.9825π nm^3, and thus, the surface areas of the slit pore, square pore, triangle pore, and the circle pore are 38.0038, 28.2351, 27.7895, and 25.0220 nm^2, respectively, as shown in Table 2. The adsorption isotherms of methane on shale kerogen are simulated by the GCMC method, and the COMPASS (Sun 1998) force field is adopted for all simulations. For the nonbonding interactions, we use the Ewald method and the Lennard-Jones 9-6 potential to describe the electrostatic potential and the vdW interaction, respectively. In the GCMC simulation, the chemical potential is a function of fugacity. The fugacity of methane is calculated by the Peng-Robinson equation (Poling et al. 2001).

4.2 Adsorption isotherms of methane on shale

Four molecular models are constructed to study the effect of pore shapes on methane adsorption on shale kerogen. The adsorption isotherms of methane on the slit pore, square pore, triangle pore, and the circle pore of shale are calculated to study the effects of the pore structure. The absolute adsorption capacities and excess adsorption capacities are plotted in Fig. 9. The excess adsorption capacities are calculated by the following equation (Wang et al. 2018a):

$$n_e = n_a - \rho V_a / M \quad (1)$$

where n_a is the absolute adsorption capacity, mol/kg; n_e is the excess adsorption capacity, mol/kg; ρ is the equilibrium density of methane, kg/m^3; V_a is the adsorption volume, m^3/kg; M is the molar mass of methane, kg/mol.

Taken the absolute and excess adsorption isotherms of the slit pore as an example. At 30 MPa, the absolute adsorption capacities are 7.21, 6.82, 6.28, and 5.89 mmol/g at 298, 328, 358, and 388 K, respectively. This indicates that the absolute methane adsorption capacity increases with increasing pressure, while decreases with increasing temperature. This is because the adsorption of methane on shale is an exothermic process (Hao et al. 2013). The absolute adsorption increases sharply at low pressures. However, with increasing pressure, the absolute adsorption increases slowly. This indicates that as the pressure decreases, the methane desorption increases. In the shale gas production, the loss of production due to decreased reservoir pressure is compensated by desorption of adsorbed gas, which may be one of the reasons that the shale gas maintains a long-term stable production (Wang et al. 2018b). For excess adsorption of methane, with increasing pressure, the excess adsorption increases, and then decreases gradually to converge. The adsorption capacities of methane on other shapes of shale pores also follow this trend.

4.3 Analysis of pore structure effects

The pore structure affects the methane adsorption on shale. In this section, we study the effect of pore shape on methane adsorption on shale nano-pores. Figure 10 depicts the absolute and excess adsorption of methane on different pores of kerogen. The absolute adsorption at 30 MPa on triangle pore is 7.93 mmol/g at 298 K, and that on the slit pore, square pore, and the circle pore are 7.21, 7.30, and 7.46 mmol/g, respectively. The adsorption capacity of methane on the triangle pore is larger than that on the slit pore, square pore, and the circle pore. This phenomenon is also observed for carbon pore structures (Song et al. 2018). Specifically, compared with the adsorption capacity of methane on the triangle pore, the adsorption capacity of methane on the slit

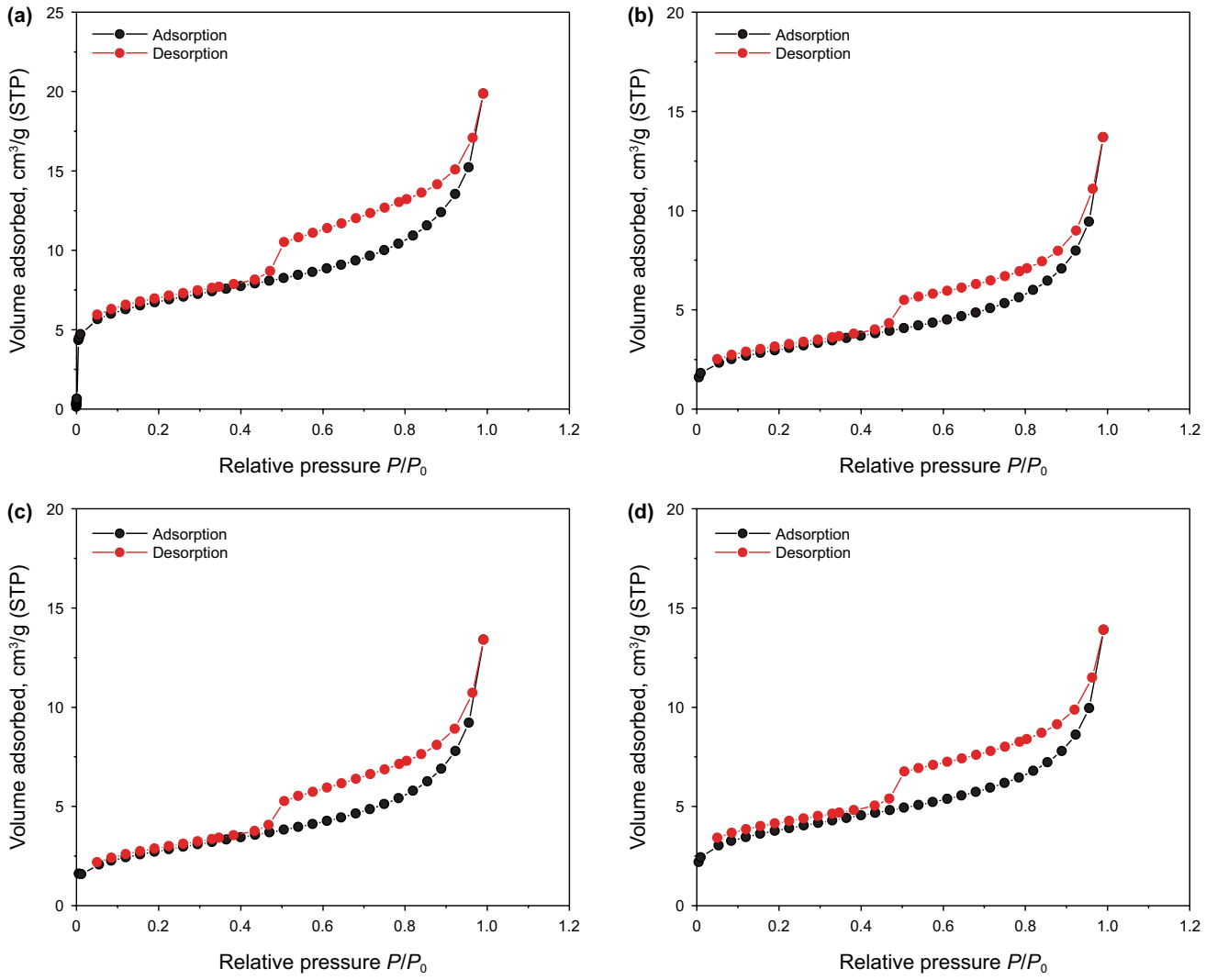

Fig. 4 N_2 adsorption–desorption isotherms of shale samples. **a** L-1; **b** L-2; **c** L-3; **d** L-4

Table 1 Pore structure parameters of shale samples

Sample No.	Specific surface area, $m^2\ g^{-1}$	Pore volume, $cm^3\ g^{-1}$	Average pore diameter, nm	Micropore volume, $cm^3\ g^{-1}$
L-1	22.84	2.27×10^{-2}	3.97	4.59×10^{-3}
L-2	10.52	1.38×10^{-2}	5.23	7.66×10^{-4}
L-3	9.83	1.34×10^{-2}	5.44	3.19×10^{-4}
L-4	12.93	1.46×10^{-2}	4.50	1.59×10^{-3}

pore, square pore, and the circle pore are reduced by 9.86%, 8.55%, and 6.12%, respectively. The adsorption capacity of methane on the triangle pore is larger than that on the slit pore, square pore, and the circle pore. Figure 11 depicts the distributions of methane molecules in four different pores at 1 MPa and 388 K. Methane molecules distribute randomly in slit pores, as shown in Fig. 11a. Particularly, Fig. 11b, c indicates that methane molecules prefer to adsorb near the corner. In Fig. 11d, we can see that methane molecules adsorb on the surface of the circle pore. The main difference between the triangle pore and other shapes is that the presence of acute angles which form wedges along the pore length. With increasing pressure, the acute wedges fill in a manner different from the right or obtuse angles found in the

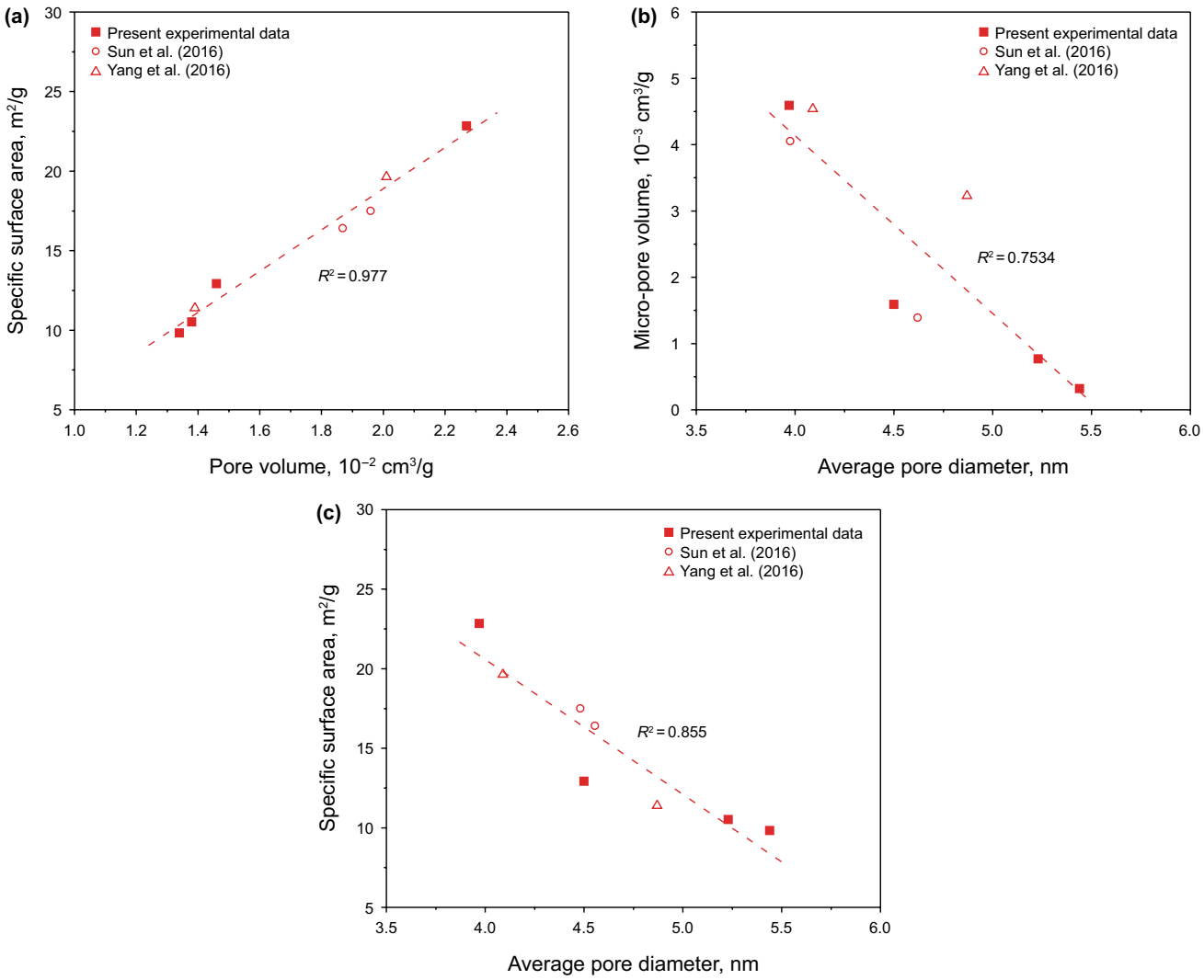

Fig. 5 Relationship of pore structure parameters of shale. **a** Specific surface area and pore volume; **b** Micro-pore volume and average pore diameter; **c** Specific surface area and average pore diameter

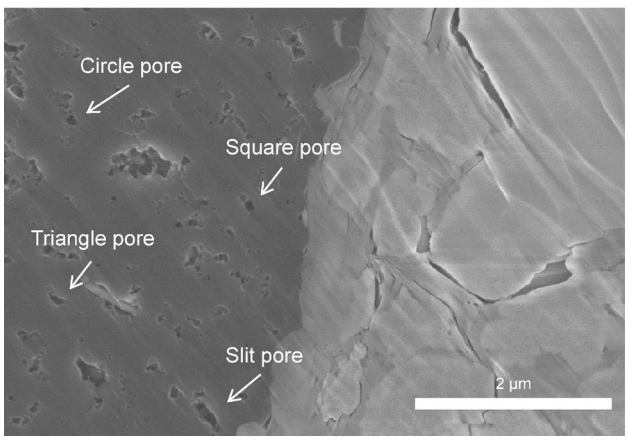

Fig. 6 Diversity of nanopores in shale kerogen

other pores (Malanoski and van Swol 2002b). It is also presented by Malanoski and van Swol (2002a) that more adsorbent adsorbed near the acute angle corner, which results in the reduction of variation in the curvature of the pore film. Figure 12 depicts the methane distributions in triangle pores at different pressures. It can be noticed that methane molecules adsorb in both the kerogen matrix and triangle pores. Particularly, Fig. 12b indicates that methane molecules prefer to adsorb near the corner at low pressures. With the pressure increases, the methane adsorption in the triangle pore increases, and there are more methane molecules adsorbed in the center area of triangle pores. The excess adsorption isotherms simulated by the Song et al. (2018) show a notable difference for different pore structures. This is because different pore structures have different pore volumes. The pore volume amplifies the difference between absolute

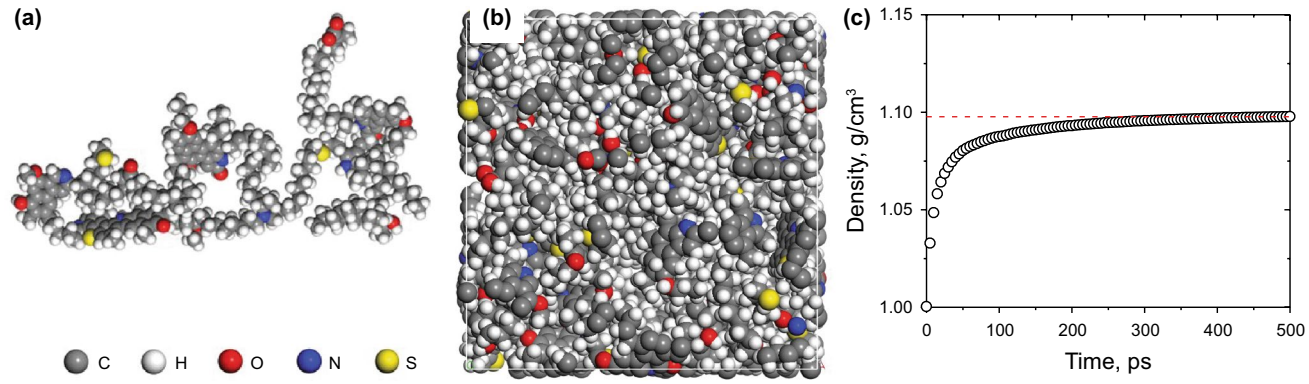

Fig. 7 **a** Kerogen molecule used in this work; **b** Model of the kerogen cell; **c** Density of the kerogen cell

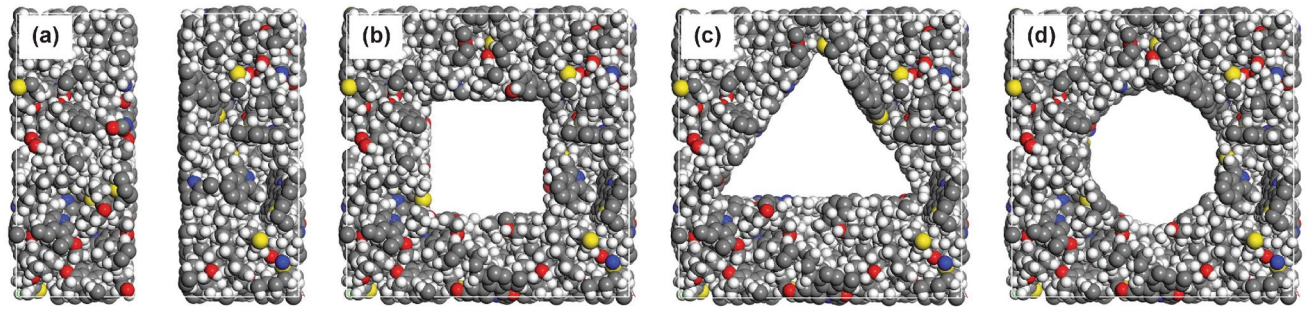

Fig. 8 Visualization of constructed kerogen pore structures. **a** Slit pore; **b** Square pore; **c** Triangle pore; **d** Circle pore

Table 2 Pore structure parameters of shale samples

Pore shape	Pore volume, nm^3	Surface area[a], nm^2
Slit pore	3.9825π	38.0038
Square pore	3.9825π	28.2351
Triangle pore	3.9825π	27.7895
Circle pore	3.9825π	25.0220

[a]Surface area is rounded to four decimal places

adsorption and excess adsorption, and the effect causes a significant decrease in the excess adsorption of circle and square pores. In the present work, because the effect of the pore volume is eliminated, the excess adsorption on shales with different pore structures have slight different values. As the temperature increases, the differences between the adsorption of various shapes decrease gradually. When the gas temperature rises to 388 K, the adsorption capacities of methane on the slit pore, square pore, and the circle pore are reduced by 4.23%, 7.61%, and 4.64%, respectively. This can be explained by the fact that the effect of temperature is more prominent with high adsorption capacity.

To quantify the effect of the water content on adsorption capacities of methane on different shaped pores, methane adsorption at 30 MPa is simulated, as shown in Fig. 13a. Compared with the results of previous research (Gasparik et al. 2013; Zhang et al. 2014; Zhao et al. 2017), water contents in moisture kerogen models are 0.6, 1.2, 1.8 and 2.4 wt%, respectively. The methane adsorption on all different pores decreases with increasing water content. Taken the methane adsorption in the triangle pore as an example, in 0.6, 1.2, 1.8, and 2.4 wt% moisture kerogen models, the methane adsorption capacities are 7.58, 7.31, 6.89, and 6.67 mmol/g, respectively, at 30 MPa. Compared with the adsorption capacity of methane on the kerogen model without water, the adsorption capacities on the moisture kerogen models reduce by 4.22%, 7.62%, 12.94%, and 15.67%, respectively. The pore shapes also affect the adsorption capacity of methane on moisture kerogen models. The adsorption of methane on the triangle pores is less affected by water content than other pore shapes. For different pore shapes, the methane adsorption capacities decrease by about 18.47%, 17.20%, 15.74%, and 17.40%, respectively on the slit pore, square pore, triangle pore, and circle pore models with a water content of 2.4 wt% at 388 K. This is because the triangle pores have the largest methane adsorption capacity without the water content. Wang et al. did simulations (Wang et al. 2018b) to investigate the effects of water content on methane adsorption and concluded that water molecules adsorb in the kerogen matrix and decrease the pore volume.

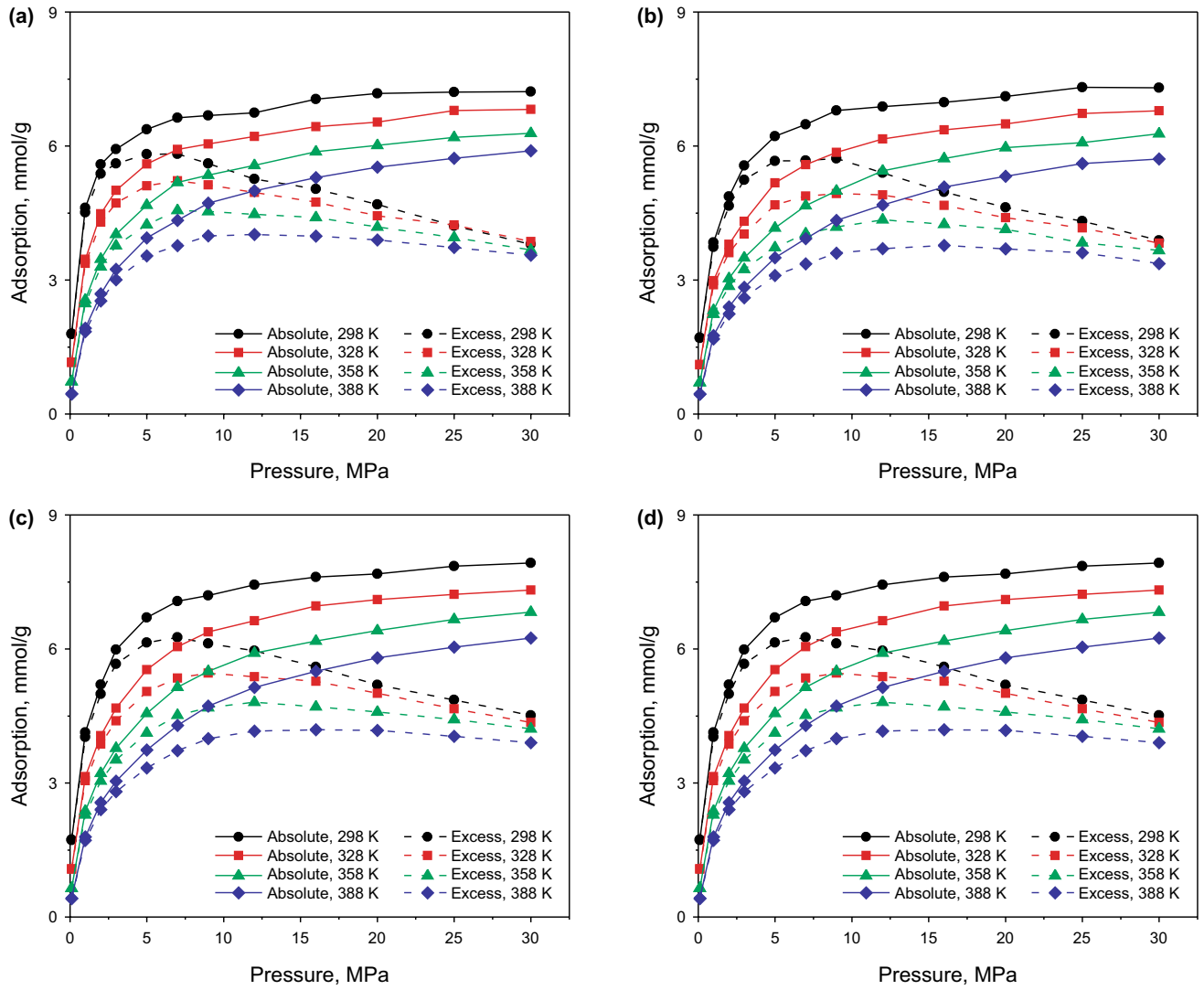

Fig. 9 Absolute and excess adsorption isotherms at different temperatures. **a** Slit pore; **b** Square pore; **c** Triangle pore; **d** Circle pore

5 Conclusions

A series of experimental techniques, such as SEM, 3D scanning confocal microscopy, X-ray nano-CT, and low-pressure N_2 adsorption analysis, are performed on the shale samples to characterize pore structures. Additionally, the adsorption behavior of methane on shale with different pore structures are studied by GCMC simulations. Through the experimental and simulation studies, major findings are summarized as follows.

(1) The distinction between the organic matter and inorganic matter is obvious, which indicates that shale is highly heterogeneous at the micro-scale. Carbon is a major component of the organic matter of shale, while the inorganic matter surface is rich in oxygen. In addition, four different pores are observed on the SEM image of the shale sample, including slit pore, square pore, triangle pore, and circle pore.

(2) The radii of most of the pores and throats are less than a micron, including the organic pores and inorganic pores in shale media. The peak values of the radii of pores and throats are 8.22×10^{-8} m and 1.46×10^{-7} m, respectively. The average coordination number is 4.21 and the distribution of coordination numbers demonstrates that there are some pores with high connectivity.

(3) Compared with the adsorption capacity of methane on triangle pores, the adsorption capacity of methane on

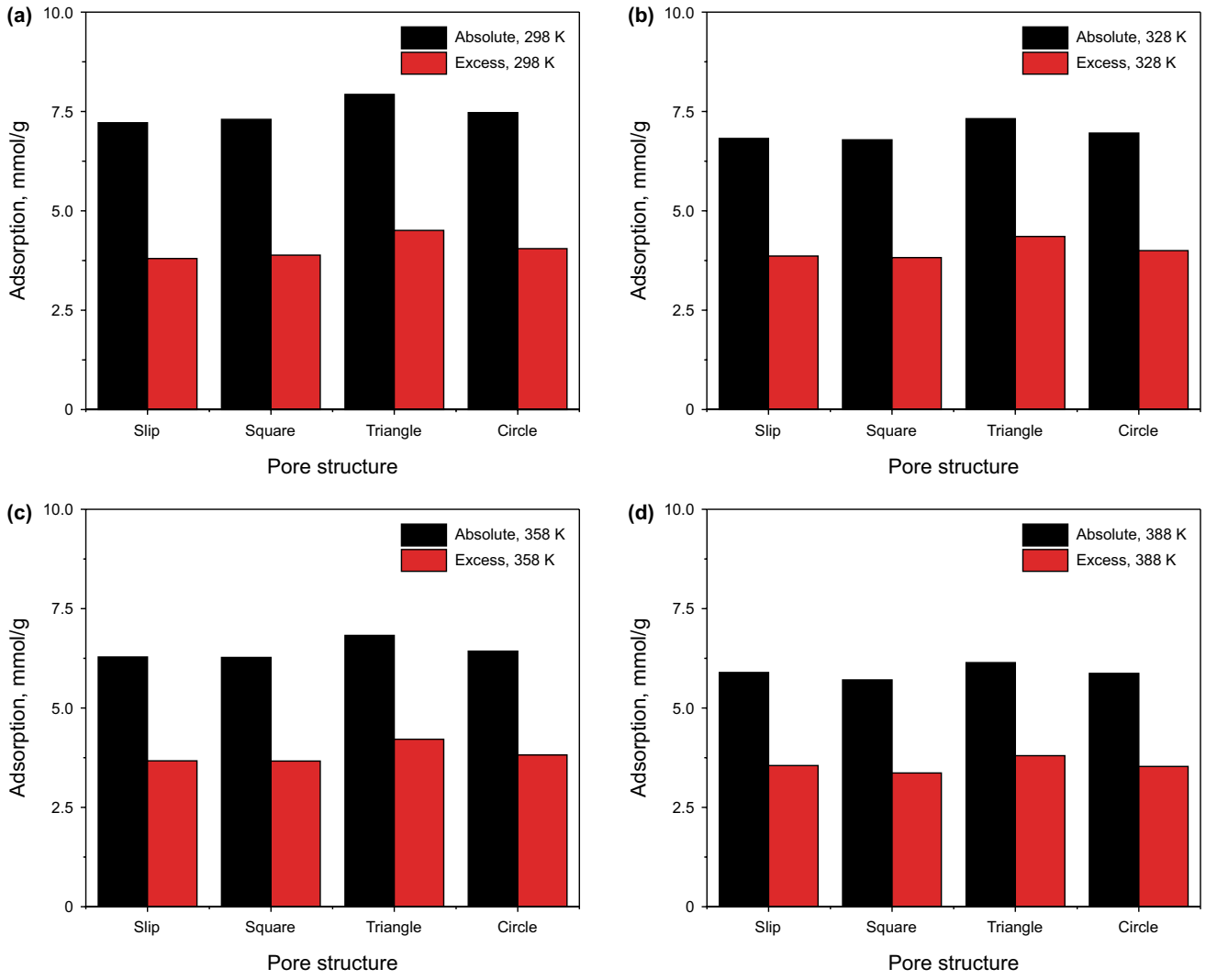

Fig. 10 Absolute and excess adsorption of methane on different pores of kerogen. **a** 298 K; **b** 328 K; **c** 358 K; **d** 388 K

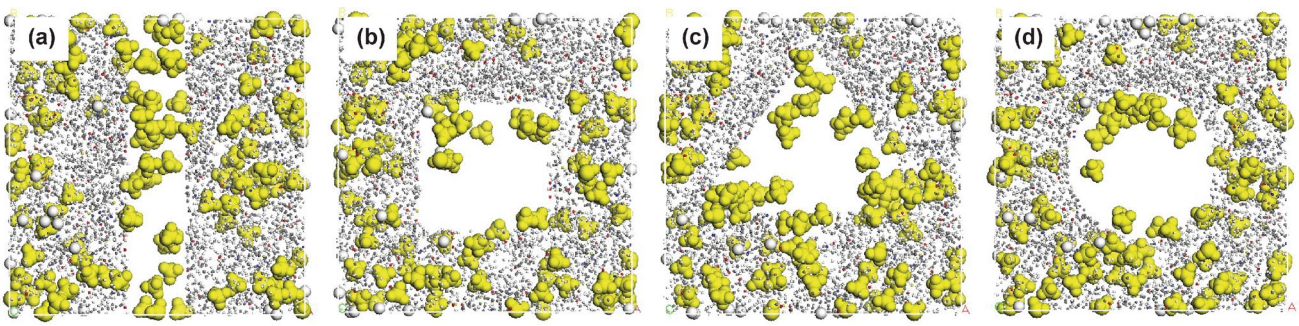

Fig. 11 Snapshots of the methane in different pores. **a** Slit pore; **b** Square pore; **c** Triangle pore; **d** Circle pore. The yellow part represents methane and to facilitate the observation, we magnified the methane molecules

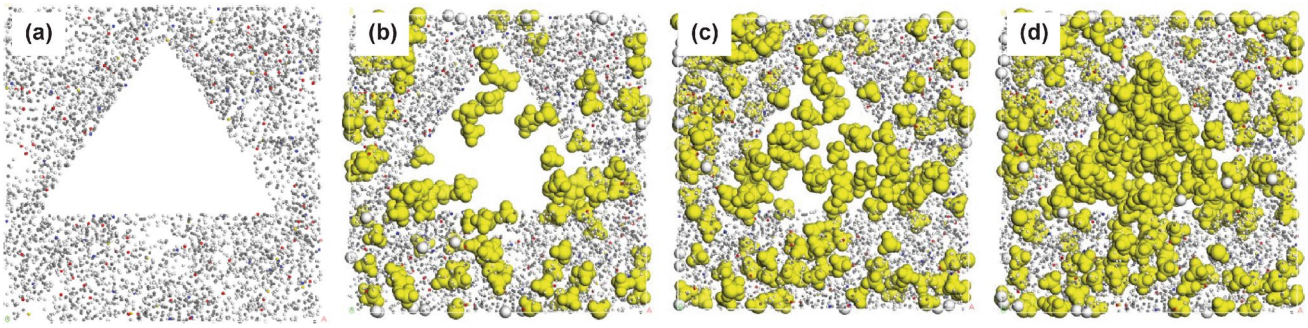

Fig. 12 Snapshots of the methane in the triangle pores. **a** No adsorption; **b** 1 MPa; **c** 2 MPa; **d** 9 MPa. The yellow part represents methane and to facilitate the observation, we magnified the methane molecules

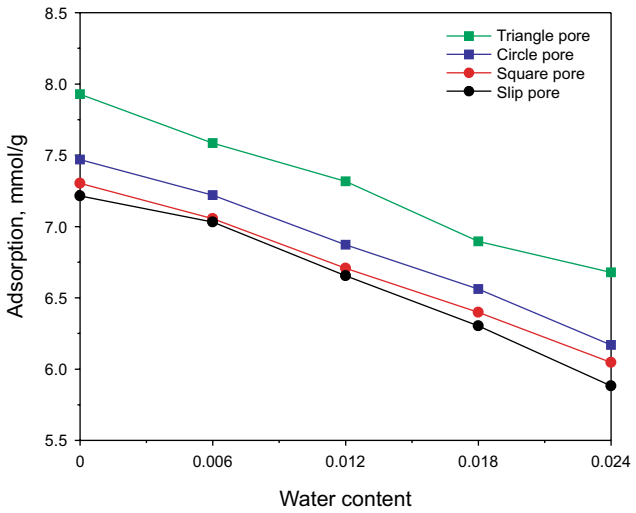

Fig. 13 The effect of the water content on methane adsorption on different pores

slit pore, square pore, and circle pore is reduced by 9.86%, 8.55%, and 6.12%, respectively. With increasing pressure, these acute wedges fill in a manner different from the right or obtuse angles found in the other pores. As the temperature increases, the differences between the adsorption on various structures decrease gradually. When the gas temperature rises to 388 K, the adsorption capacity of methane on the slit pore, square pore, and the circle pore is reduced by 4.23%, 7.61%, and 4.64%, respectively.

(4) Methane adsorption on all different pores decreases with increasing water content. The adsorption of methane adsorption on triangle pores is less affected by the water content than other pore shapes.

Acknowledgements The authors acknowledge financial support from the Science Fund for Creative Research Groups of the National Natural Science Foundation of China (No. 51821092), the General Projects of the Natural Science Foundation of China (No. 51674275) and the Foundation of State Key Laboratory of Petroleum Resources and Prospecting, China University of Petroleum, Beijing (No. PRP/open-2003). Tianyu Wang acknowledges the China Scholarship Council for financial support during his visit to Harvard University.

References

Al-Kharusi AS, Blunt MJ. Network extraction from sandstone and carbonate pore space images. J Pet Sci Eng. 2007;56(4):219–31. https://doi.org/10.1016/j.petrol.2006.09.003.

Chalmers GR, Bustin RM, Power IM. Characterization of gas shale pore systems by porosimetry, pycnometry, surface area, and field emission scanning electron microscopy/transmission electron microscopy image analyses: examples from the Barnett, Woodford, Haynesville, Marcellus, and Doig units characterization of gas shale pore systems. AAPG Bull. 2012;96(6):1099–119. https://doi.org/10.1306/10171111052.

Chen L, Zuo L, Jiang Z, Jiang S, Liu K, Tan J, Zhang L. Mechanisms of shale gas adsorption: evidence from thermodynamics and kinetics study of methane adsorption on shale. Chem Eng J. 2019;361:559–70. https://doi.org/10.1016/j.cej.2018.11.185.

Clarkson CR, Solano N, Bustin RM, Bustin A, Chalmers G, He L, Melnichenko YB, Radliński A, Blach TP. Pore structure characterization of North American shale gas reservoirs using USANS/SANS, gas adsorption, and mercury intrusion. Fuel. 2013;103:606–16. https://doi.org/10.1016/j.fuel.2012.06.119.

Curtis JB. Fractured shale-gas systems. AAPG Bull. 2002;86(11):1921–38. https://doi.org/10.1306/61EEDDBE-173E-11D7-8645000102C1865D.

Dong H, Blunt MJ. Pore-network extraction from micro-computerized-tomography images. Phys Rev E. 2009;80(3):036307. https://doi.org/10.1103/PhysRevE.80.036307.

Feng D, Li X, Wang X, Li J, Sun F, Sun Z, Zhang T, Li P, Chen Y, Zhang X. Water adsorption and its impact on the pore structure characteristics of shale clay. Appl Clay Sci. 2018;155:126–38. https://doi.org/10.1016/j.clay.2018.01.017.

Gasparik M, Ghanizadeh A, Gensterblum Y, Krooss BM. "Multi-temperature" method for high-pressure sorption measurements on moist shales. Rev Sci Instrum. 2013;84(8):085116. https://doi.org/10.1063/1.4817643.

Gensterblum Y, Busch A, Krooss BM. Molecular concept and experimental evidence of competitive adsorption of H_2O, CO_2 and CH_4 on organic material. Fuel. 2014;115:581–8. https://doi.org/10.1016/j.fuel.2013.07.014.

Groen JC, Peffer LA, Pérez-Ramírez J. Pore size determination in modified micro-and mesoporous materials. Pitfalls and limitations in gas adsorption data analysis. Microporous Mesoporous Mater. 2003;60(1–3):1–17. https://doi.org/10.1016/S1387-1811(03)00339-1.

Hao F, Zou H, Lu Y. Mechanisms of shale gas storage: implications for shale gas exploration in China. AAPG Bull. 2013;97(8):1325–46. https://doi.org/10.1306/02141312091.

Hughes JD. A reality check on the shale revolution. Nature. 2013;494:307. https://doi.org/10.1038/494307a.

Javadpour F, Moravvej Farshi M, Amrein M. Atomic-force microscopy: a new tool for gas-shale characterization. J Canad Pet Technol. 2012;51(04):236–43. https://doi.org/10.2118/161015-PA.

Jin Z, Firoozabadi A. Effect of water on methane and carbon dioxide sorption in clay minerals by Monte Carlo simulations. Fluid Phase Equilib. 2014;382:10–20. https://doi.org/10.1016/j.fluid.2014.07.035.

Kelemen S, Afeworki M, Gorbaty M, Sansone M, Kwiatek P, Walters C, Freund H, Siskin M, Bence A, Curry D. Direct characterization of kerogen by X-ray and solid-state ^{13}C nuclear magnetic resonance methods. Energy Fuels. 2007;21(3):1548–61. https://doi.org/10.1021/ef060321h.

Krooss BV, Van Bergen F, Gensterblum Y, Siemons N, Pagnier H, David P. High-pressure methane and carbon dioxide adsorption on dry and moisture-equilibrated Pennsylvanian coals. Int J Coal Geol. 2002;51(2):69–92. https://doi.org/10.1016/S0166-5162(02)00078-2.

Liu Y, Wilcox J. Molecular simulation studies of CO_2 adsorption by carbon model compounds for carbon capture and sequestration applications. Environ Sci Technol. 2012;47(1):95–101. https://doi.org/10.1021/es3012029.

Loucks RG, Reed RM, Ruppel SC, Hammes U. Spectrum of pore types and networks in mudrocks and a descriptive classification for matrix-related mudrock pores. AAPG Bull. 2012;96(6):1071–98. https://doi.org/10.1306/08171111061.

Malanoski A, van Swol F. Lattice density functional theory investigation of pore shape effects. I. Adsorption in single nonperiodic pores. Phys Rev E. 2002a;66(4):041602. https://doi.org/10.1103/PhysRevE.66.041602.

Malanoski A, van Swol F. Lattice density functional theory investigation of pore shape effects. II. Adsorption in collections of noninterconnected pores. Phys Rev E. 2002b;66(4):041603. https://doi.org/10.1103/PhysRevE.66.041603.

Mastalerz M, He L, Melnichenko YB, Rupp JA. Porosity of coal and shale: insights from gas adsorption and SANS/USANS techniques. Energy Fuels. 2012a;26(8):5109–20. https://doi.org/10.1021/ef300735t.

Mastalerz M, Schimmelmann A, Lis G, Drobniak A, Stankiewicz A. Influence of maceral composition on geochemical characteristics of immature shale kerogen: insight from density fraction analysis. Int J Coal Geol. 2012b;103:60–9. https://doi.org/10.1016/j.coal.2012.07.011.

Poling BE, Prausnitz JM, John Paul OC, Reid RC. The properties of gases and liquids, 5. McGraw-Hill New York. 2001.

Ren W, Li G, Tian S, Sheng M, Fan X. An analytical model for real gas flow in shale nanopores with non-circular cross-section. AIChE J. 2016;62(8):2893–901. https://doi.org/10.1002/aic.15254.

Ren W, Li G, Tian S, Sheng M, Geng L. Adsorption and surface diffusion of supercritical methane in shale. Ind Eng Chem Res. 2017. https://doi.org/10.1021/acs.iecr.6b04432.

Ross DJ, Bustin RM. Characterizing the shale gas resource potential of Devonian-Mississippian strata in the Western Canada sedimentary basin: application of an integrated Formation evaluation. AAPG Bull. 2008;92(1):87–125. https://doi.org/10.1306/09040707048.

Sharma A, Namsani S, Singh JK. Molecular simulation of shale gas adsorption and diffusion in inorganic nanopores. Mol Simul. 2015;41(5–6):414–22. https://doi.org/10.1080/08927022.2014.968850.

Shen W, Song F, Hu X, Zhu G, Zhu W. Experimental study on flow characteristics of gas transport in micro-and nanoscale pores. Sci Rep. 2019;9(1):1–10. https://doi.org/10.1038/s41598-019-46430-2.

Shi Y, Song X, Wang G, McLennan J, Forbes B, Li X, Li J. Study on wellbore fluid flow and heat transfer of a multilateral-well CO_2 enhanced geothermal system. Appl Energy. 2019;249:14–27. https://doi.org/10.1016/j.apenergy.2019.04.117.

Sing KS. Reporting physisorption data for gas/solid systems with special reference to the determination of surface area and porosity (Recommendations 1984). Pure Appl Chem. 1985;57(4):603–19.

Singh H, Cai J. A mechanistic model for multi-scale sorption dynamics in shale. Fuel. 2018;234:996–1014. https://doi.org/10.1016/j.fuel.2018.07.104.

Song W, Yao J, Ma J, Li A, Li Y, Sun H, Zhang L. Grand canonical Monte Carlo simulations of pore structure influence on methane adsorption in micro-porous carbons with applications to coal and shale systems. Fuel. 2018;215:196–203. https://doi.org/10.1016/j.fuel.2017.11.016.

Sun H. COMPASS: an ab initio force-field optimized for condensed-phase applications overview with details on alkane and benzene compounds. J Phys Chem B. 1998;102(38):7338–64. https://doi.org/10.1021/jp980939v.

Sun M, Yu B, Hu Q, Chen S, Xia W, Ye R. Nanoscale pore characteristics of the Lower Cambrian Niutitang Formation Shale: a case study from Well Yuke# 1 in the Southeast of Chongqing, China. Int J Coal Geol. 2016;154:16–29. https://doi.org/10.1016/j.coal.2015.11.015.

Tian S, Dong X, Wang T, Zhang R, Zhang P, Sheng M, Cheng S, Zhao H, Fei L, Street J. Surface properties of organic kerogen in continental and marine shale. Langmuir. 2018;34(46):13882–7. https://doi.org/10.1021/acs.langmuir.8b03151.

Tian S, Wang T, Li G, Sheng M, Zhang P. Nanoscale surface properties of organic matter and clay minerals in shale. Langmuir. 2019;35(17):5711–8. https://doi.org/10.1021/acs.langmuir.9b00157.

Tiwari P, Deo M, Lin C, Miller J. Characterization of oil shale pore structure before and after pyrolysis by using X-ray micro CT. Fuel. 2013;107:547–54. https://doi.org/10.1016/j.fuel.2013.01.006.

Ungerer P, Collell J, Yiannourakou M. Molecular modeling of the volumetric and thermodynamic properties of kerogen: influence of organic type and maturity. Energy Fuels. 2014;29(1):91–105. https://doi.org/10.1021/ef502154k.

Vidic RD, Brantley SL, Vandenbossche JM, Yoxtheimer D, Abad JD. Impact of shale gas development on regional water quality. Science. 2013;340(6134):1235009. https://doi.org/10.1126/science.1235009.

Wang S, Feng Q, Javadpour F, Hu Q, Wu K. Competitive adsorption of methane and ethane in montmorillonite nanopores of shale at supercritical conditions: a grand canonical Monte Carlo simulation study. Chem Eng J. 2019a;355:76–90. https://doi.org/10.1016/j.cej.2018.08.067.

Wang T, Tian S, Li G, Sheng M. Selective adsorption of supercritical carbon dioxide and methane binary mixture in shale kerogen nanopores. J Nat Gas Sci Eng. 2018a;50:181–8. https://doi.org/10.1016/j.jngse.2017.12.002.

Wang T, Tian S, Li G, Sheng M, Ren W, Liu Q, Zhang S. Molecular simulation of CO_2/CH_4 competitive adsorption on shale kerogen for CO_2 sequestration and enhanced gas recovery. J Phys Chem C. 2018b;122(30):17009–18. https://doi.org/10.1021/acs.jpcc.8b02061.

Wang T, Tian S, Li G, Sheng M, Ren W, Liu Q, Tan Y, Zhang P. Experimental study of water vapor adsorption behaviors on shale. Fuel. 2019b;248:168–77. https://doi.org/10.1016/j.fuel.2019.03.029.

Wei M, Zhang L, Xiong Y, Li J, Peng PA. Nanopore structure characterization for organic-rich shale using the non-local-density functional theory by a combination of N_2 and CO_2 adsorption. Microporous Mesoporous Mater. 2016;227:88–94. https://doi.org/10.1016/j.micromeso.2016.02.050.

Wu H, Chen J, Liu H. Molecular dynamics simulations about adsorption and displacement of methane in carbon nanochannels. J Phys Chem C. 2015;119(24):13652–7. https://doi.org/10.1021/acs.jpcc.5b02436.

Xiong J, Liu X, Liang L. Experimental study on the pore structure characteristics of the upper ordovician Wufeng Formation shale in the southwest portion of the Sichuan basin, China. J Nat Gas Sci Eng. 2015;22:530–9. https://doi.org/10.1016/j.jngse.2015.01.004.

Xiong J, Liu X, Liang L, Zeng Q. Methane adsorption on carbon models of the organic matter of organic-rich shales. Energy Fuels. 2017;31(2):1489–501. https://doi.org/10.1021/acs.energyfuels.6b03144.

Yang F, Ning Z, Wang Q, Zhang R, Krooss BM. Pore structure characteristics of lower Silurian shales in the southern Sichuan Basin, China: insights to pore development and gas storage mechanism. Int J Coal Geol. 2016;156:12–24. https://doi.org/10.1016/j.coal.2015.12.015.

Yuan Q, Zhu X, Lin K, Zhao Y-P. Molecular dynamics simulations of the enhanced recovery of confined methane with carbon dioxide. Phys Chem Chem Phys. 2015;17(47):31887–93. https://doi.org/10.1039/C5CP06649B.

Yuan W, Pan Z, Li X, Yang Y, Zhao C, Connell LD, Li S, He J. Experimental study and modelling of methane adsorption and diffusion in shale. Fuel. 2014;117:509–19. https://doi.org/10.1016/j.fuel.2013.09.046.

Zhai Z, Wang X, Jin X, Sun L, Li J, Cao D. Adsorption and diffusion of shale gas reservoirs in modeled clay minerals at different geological depths. Energy Fuels. 2014;28(12):7467–73. https://doi.org/10.1021/ef5023434.

Zhang J, Clennell M, Dewhurst D, Liu K. Combined Monte Carlo and molecular dynamics simulation of methane adsorption on dry and moist coal. Fuel. 2014;122:186–97. https://doi.org/10.1016/j.fuel.2014.01.006.

Zhang P, Hu L, Meegoda JN, Gao S. Micro/nano-pore network analysis of gas flow in shale matrix. Sci. Rep. 2015;5(1):1–11. https://doi.org/10.1038/srep13501.

Zhao T, Li X, Zhao H, Li M. Molecular simulation of adsorption and thermodynamic properties on type II kerogen: influence of maturity and moisture content. Fuel. 2017;190:198–207. https://doi.org/10.1016/j.fuel.2016.11.027.

Zhou S, Ning Y, Wang H, Liu H, Xue H. Investigation of methane adsorption mechanism on Longmaxi shale by combining the micropore filling and monolayer coverage theories. Adv Geo-Energy Res. 2018;2(3):269–81. https://doi.org/10.26804/ager.2018.03.05.

Zou J, Rezaee R, Xie Q, You L, Liu K, Saeedi A. Investigation of moisture effect on methane adsorption capacity of shale samples. Fuel. 2018;232:323–32. https://doi.org/10.1016/j.fuel.2018.05.167.